frontiers | Frontiers in Environmental Science

TYPE Original Research
PUBLISHED 13 September 2022
DOI 10.3389/fenvs.2022.994152

OPEN ACCESS

EDITED BY
Haibo Li,
Northeastern University, China

REVIEWED BY
Lei Luo,
Chinese Academy of Sciences (CAS), China
Yu Shen,
Chongqing Technology and Business University, China
Zongqiang Gong,
Institute of Applied Ecology (CAS), China

*CORRESPONDENCE
Yun Zhang,
zhangyun1977@syau.edu.cn

SPECIALTY SECTION
This article was submitted to Toxicology, Pollution and the Environment, a section of the journal Frontiers in Environmental Science

RECEIVED 14 July 2022
ACCEPTED 29 August 2022
PUBLISHED 13 September 2022

CITATION
Feng S, Yan Z, Ni Q and Zhang Y (2022), In-situ synthesis of 3D BiOBr/UiO-66-NH_2 heterojunction nanocomposite and its excellent photocatalytic degradation of rhodamine B dye. *Front. Environ. Sci.* 10:994152. doi: 10.3389/fenvs.2022.994152

In-situ synthesis of 3D BiOBr/UiO-66-NH_2 heterojunction nanocomposite and its excellent photocatalytic degradation of rhodamine B dye

Shuna Feng[1,2], Zheng Yan[2], Qianqian Ni[2] and Yun Zhang[1]*

[1]Northeast Key Laboratory of Arable Land Conservation and Improvement, Ministry of Agriculture, College of Land and Environment, Shenyang Agricultural University, Shenyang, China, [2]Liaoning Key Laboratory of Clean Energy and College of Energy and Environmental, Shenyang Aerospace University, Shenyang, China

As a primary goal, The fast recombination of stimulated excitons and poor visible light response are key problems in the photocatalysis field. Combining with materials with good visible light responses to form heterogeneous structures is still the most effective way. In this study, BiOBr/UiO-66-NH_2 photocatalyst was synthesized by a simple method. BiOBr is a 3D spherical structure stacked by nanosheets, which enhance its adsorption capacity for pollutants and catalyze the dark reaction to reach the equilibrium point for too long. Coupling with UiO-66-NH_2, its adsorption capacity was inhibited and the dark reaction time was shortened. The excellent removal rate of Rhodamine B (RhB) by BiOBr/UiO-66-NH_2 reached 96.79% after 30 min of visible light irradiation and 99.37% after 90 min. With an increase in pollutant concentration, the composite still showed excellent photocatalytic performance. This study also tried to abandon the dark adsorption stage and directly degraded RhB efficiently and quickly under visible light. Finally, the photocatalytic enhancement mechanism was proposed.

KEYWORDS

BiOBr/UiO-66-NH_2, heterojunction, photocatalysis, rhodamine B, *in-situ* synthesis

Introduction

With the continuous development of textile, papermaking, printing and other industries, dyes are discharged into the water environment with wastewater, which poses a threat to human health and water quality. The degradation of dyes in water has attracted widespread attention (Bhatt et al., 2012). RhB, as a common dye in dye wastewater, has caused great damage to the environment. It is difficult to degrade and toxic. It exists in the water environment for a long time, which will affect the self-purification capacity of water and threaten human health through the food chain (Xia et al., 2021). According to previous studies, photocatalytic technology has proved to be an effective method for degrading dyes (Bargozideh et al., 2020; Chen et al., 2020; Sun et al.,

2020; Wen et al., 2020). Under the excitation of light, the carriers produced by photocatalysts can react with H_2O and O_2 to produce reactive oxygen species (ROS), which can react with dyes to achieve the purpose of degradation.

Metal-organic frameworks (MOFs) have great potential in photocatalysis due to their advantages of large specific surface area, high porosity and good thermal stability (Zeng et al., 2016; Xu et al., 2018). UiO-66-NH_2 exhibits large surface area and excellent thermochemical stability due to its strong Zr-O bond and high Zr coordination number (Wu et al., 2013). The large surface area of MOFs not only facilitates the adsorption of pollutants but, in addition, MOFs can be used as a carrier to improve the dispersity of the catalyst. UiO-66-NH_2 is a typical MOF, and it also has good visible light responsiveness (Yang et al., 2019; Liu et al., 2022). However, due to its rapid charge recombination, its photocatalytic performance is poor (Fan et al., 2021). At present, heterojunction construction can inhibit the recombination of electron hole pairs generated by photoexcitation, improve the efficiency of photocatalytic degradation of pollutants and improve the visible light response ability of materials (Zhang et al., 2019).

Bismuthoxyhalide BiOX (X = Cl, Br, I) has been widely studied in the field of photocatalysis in recent years due to its suitable band gap and unique layered structure (Hao et al., 2020; Yang et al., 2020; Han et al., 2021). BiOBr, as a typical bismuthoxyhalide, has the advantages of low cost, environmental friendliness and easy material acquisition. It is a promising photocatalyst. BiOBr has many of the same problems as most photocatalysts: 1) poor visible light response and 2) fast photoexcited electron hole recombination (Chen et al., 2019; Yang et al., 2021). In addition, BiOBr has revealed other problems as research has progressed. It is well known that the ultimate photocatalytic performance of materials is also influenced by morphology, with 3D structures exposing more active sites than nanosheets (2D). BiOBr with a unique 3D spherical structure can be synthesized by the solvothermal method and the simple *in situ* deposition method (Shi et al., 2019; Yang et al., 2019). Many studies have shown that the catalyst prepared by the *in situ* direct growth method has stronger intermolecular force and more abundant reaction sites than other methods, thus showing higher catalytic activity (Zhou et al., 2020). However, some BiOBr (3D) synthesized by the *in situ* deposition method has a large surface area, a large proportion of mesopores and a large number of gaps formed by the accumulation of nanosheets, which make BiOBr have a strong adsorption capacity for pollutants and take too long to reach the equilibrium point of adsorption and desorption, further prolonging the overall reaction time. On the other hand, the degradation effect of BiOBr due to its adsorption capacity is stronger than that of photodegradation on the whole. This property does not accord with the photocatalytic reaction in which the photocatalytic stage is the main stage of degradation (Yang et al., 2019; Wang et al., 2021). More importantly, BiOBr is consistent with other materials, but its adsorption capacity cannot be well inhibited, and it will interfere with the determination of BiOBr composite photocatalytic degradation capacity of pollutants.

The goal of this study was to develop a photocatlytic material with 3D structure based on UiO-66-NH_2 to efficientlt degrade RhB. The physicochemical properties of the materials were characterized in different ways. The photocatalytic degradation of RhB by the composite was investigated under simulated visible light. In addition, by changing the concentration of pollutants and abandoning the dark adsorption stage, the visible light degradation of RhB was directly carried out to explore the photocatalytic performance of the prepared catalyst, providing data support for the practical application of the catalyst. Finally, the active species affecting the photocatalytic activity were studied and the enhancement photodegradation mechanism of RhB was proposed.

Experimental methods

Materials

Chemical reagents: Zirconium chloride ($ZrCl_4$), 2-amino-1, 4-benzenedicarboxylic acid (NH_2-BDC), N, N-Dimethylformamide (DMF), glacial acetic acid, bromatum kalium (KBr), ethyleneglycol (EG), absolute methanol are in AR grade and purchased from Aladdin. Bismuth nitrate pentahydrate ($Bi(NO_3)_3{\cdot}5H_2O$) are in AR grade and purchased from Macklin. All chemical reagents were used without further purification.

Synthesis of UiO-66-NH_2

The UiO-66-NH_2 was synthesized by the previous reported procedure, with some modifications (Xu et al., 2018). 4.5 mmol $ZrCl_4$ were ultrasonically dispersed in 40.0 ml DMF. 4.5 mmol NH_2-BDC were put into the above solution and dissolved by ultrasonic dispersion. The mixed solution was stirred for 1h, and 8 ml drops of acetic acid were added. Next, the suspension was transferred to a Teflon-lined stainless steel autoclave and heated at 140°C for 24 h. After the reaction, the autoclave was slowly cooled down to room temperature and the prepared material washed with DMF and absolute methanol respectively, then dried in a vacuum freeze dryer at -60 °C.The as-synthesized UiO-66-NH_2 was denoted as U.

Synthesis of BiOBr/UiO-66-NH_2 and BiOBr

2.7441 g UiO-66-NH_2 powder was fully added into 20 ml of 0.119 g KBr solution. 0.485 g $Bi(NO_3)_3.5H_2O$ was dispersed in

20 ml EG, ultrasonic was performed for about 30 min, and stirred for 20 min. The above suspended droplets of UiO-66-NH_2 were added to the solution and stirred for 4 h. The product was centrifuged and washed with deionized water and ethanol. Then dried in a vacuum freeze dryer at -60 °C. The materials of other proportions were prepared by adjusting the dosage of UiO-66-NH_2. The as-synthesized BiOBr/UiO-66-NH_2 composite with 10 wt%, 20 wt%, 30 wt% and 50 wt% BiOBr were denoted as UB-10%, UB-20%, UB-30%, UB-50%, respectively.

BiOBr was prepared by the same method, but without the addition of UiO-66-NH_2. The as-synthesized material was denoted as B.

Characterization

X-ray diffractometer (XRD) of the as-synthesized samples was performed using a DX-2700 X-ray diffractometer using Cu Kα1 (λ = 1.5406 Å) at two theta range of 5–90°. The morphologies were analyzed by Scanning Electron Microscopy (SEM) (CarlZeiss Merlin, Germany) with integrated Oxford EDS system and Transmission Electron Microscopy (TEM) (FEI Tecnai G2 F20). N_2 adsorption-desorption isotherms were obtained at -196°Con a Micromeritics ASAP 2460 Sorptometer using static adsorption procedures, and the Brunauer–Emmett–Teller (BET) surface areas and pore size distributions were calculated by using N_2 adsorption-desorption isotherms. X-ray photoelectron spectroscopy (XPS) was detected by a Thermo ESCALAB 250XI spectrometer. UV-vis diffuse reflectance spectra (DRS) was obtained using a UV-4100 spectrometer.

Photodegradation test

The photocatalytic activity was tested via photodegradation of RhB aqueous solutions under ambient temperatures. In detail, 60 mg of the sample powder were added in 200 ml RhB aqueous solutions in a 300 ml double layer photocatalytic reactor. 300 W Xenon lamp (λ > 420 nm) was served as the light source. The concentration of RhB was 10 mg/L. The solution was kept in dark for 30 min to reach an adsorption–desorption equilibrium. 5 ml solution was taken out every 10 min and centrifuged, After centrifugation, 3 ml supernatant was taken for a second centrifugation. Then, the absorbancy of the solution was analyzed by ultraviolet spectrophotometer to determine the RhB concentration (λ = 554 nm). All experiments were repeated for 3 times and averaged for analysis. The removal efficiency of RhB by the photocatalyst was calculated by Eq. 1:

$$\eta = \frac{C_0 - C_t}{C_0} \times 100\% \quad (1)$$

Where C_0 and C_t represent the initial RhB concentration and the RhB concentration at the time of t, respectively.

Photoelectrochemical tests

The photoluminescence (PL) was measured on a Edinburgh Analytical Instruments FLs-980 spectrophotometer. The Photocurrent (PC) and Electrochemical Impedance Spectroscopy (EIS) were measured using the three-electrode electrochemical analysis on CHI 660E electrochemical workstation. The synthesized sample, Pt sheet and Hg/HgCl worked as the working, counter, and reference electrodes, respectively. 0.1 M Na_2SO_4 solution (30 ml) served as the electrolyte. The visible light irradiation (λ > 420 nm) was supplied from a 300 W Xenon lamp, and the light/dark short-circuit photocurrent was analyzed by using the open-circuit voltage as bias. To ensure reproducibility, all the experimental parameters, including temperature, the distance between light source and reaction solution, were maintained constant.

Results and discussion

Morphology analysis

The crystal structure and purity of the photocatalyst were analyzed by XRD. Figure 1 presents the XRD data for the prepared U, B, UB-10%, UB-20%, UB-30% and UB-50%. U and B all show sharp characteristic diffraction peaks, indicating that they possess higher purity. The diffraction peaks of U fit well with previous study, which exhibits characteristic peaks at 7.34°, 8.37°, 25.48°, 43.14° (Su et al., 2017). The XRD curves of composites all exhibited the major peak features of U, suggesting that the loading of B did not destroy the crystal texture of U framework, the structure of U remained stable during the synthesis of composite photocatalysts. With the increase of BiOBr concentration, the characteristic diffraction peak belonging to UiO-66-NH_2 decreases correspondingly. B exhibits the main diffraction peaks at 32.2°, 46.3°and 57.6°, which are attributed to (110), (200), 212) crystal plane (JCPDS 09-0393), respectively. The main diffraction peaks of U and B can be seen in the diffraction pattern of every composite photocatalysts, demonstrating that the successful construction of the composite material.

The SEM images of U, B and UB-30% composites are presented in Figure 2. The as-synthesized pure U consists of aggregated polyhedral particles, as shown in Figure 2A. Pure B is composed of many tightly packed irregular nanosheets, and the nanosheets come together to form nanospheres in Figure 2B. A large number of gaps formed by the accumulation of nanosheets can enhance its adsorption capacity for pollutants. Each sphere is

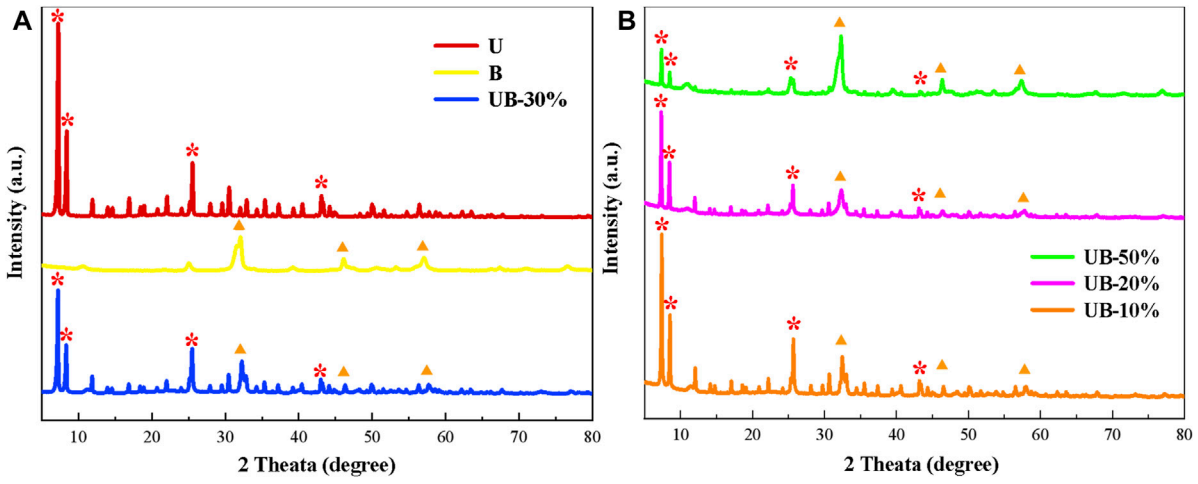

FIGURE 1
XRD patterns of U, B, UB-10%, UB-20%, UB-30% and UB-50% composites.

approximately 300–400 nm in diameter. In Figures 2C,D, it is observed that B adheres closely to U, indicating that there was an interaction between B and U. In addition, B has a good dispersion on the surface of U, and there is no phenomenon of large-area graph agglomeration. It is confirmed that U as a carrier can increase the dispersity of the surface-supported catalyst. UB-30% was studied in more detail using TEM and HRTEM, as shown in Figures 2E,F. XRD results show that BiOBr(110) has a tetragonal phase and the lattice fringe spacing is 0.28 nm, which is in good agreement with the crystal plane of BiOBr(110). Importantly, HRTEM images also show a tight interfacial connection between BiOBr and UiO-66-NH_2, suggesting the formation of a BiOBr/UiO-66-NH_2 system. As shown in Figure 2G, the composite contains characteristic elements Zr, O, C, Bi and Br of a single material and the element distributions are uniform, indicating that B is successfully loaded on the surface of U.

To study the specific surface area of as-prepared samples, the N_2 adsorption-desorption isotherms of U, B and UB-30% were acquired. As can be seen from Figures 3A–C, the as-prepared U and UB-30% all show hybrid type IV isotherms with H_4 typical hysteresis loops, indicating the existence of mesoporous structure. The as-prepared B displays a type V isotherm with a H_3 typical hysteresis loop, indicating the presence of mesoporous structure, and the H_3 hysteresis loop proves that the hole has a flat slit structure (Zhu et al., 2020), which may come from the interstitial space formed by stacking the nanosheets. The presence of intermediary pores in the three materials can be confirmed by the pore size distribution. Furthermore, the Barret-Joyner-Halenda (BJH) method was used to calculate the pore size distribution. As shown in Table 1, the BET surface area, pore volumes and pore sizes of the photocatalysts were obtained. The specific surface areas of U, B and UB-30% are 475, 36 and 581 m^2/g, respectively. The specific surface area of UB-30% composite is higher than that of U and B. The specific surface area of U is largest, which is conducive to the adsorption of RhB and can improve the dispersity of B. The large specific surface area of U causes the complex to have a large specific surface area. The average pore volumes of U, B and UB-30% are 0.14, 0.73 and 0.26 cm^3/g, respectively. The pore size of B is largest, leading to its strong adsorption capacity for pollutants. However, by comparing the pore volume and pore size of the composite with those of B, the average pore size and pore melt of the composite material become smaller, which proves that the coupling of the two materials can reduce the pore size and further inhibit the adsorption capacity of B for pollutants.

XPS chemical species of elements analysis

XPS was further used to study the chemical composition and elemental distribution of thecompounds (Figure 4). The survey spectrum shows that UB-30% is composed of Zr, O, C, Br and Bi elements which is in good agreement with the EDS results. (Figure 4A). The Bi 4f has two symmetrical peaks at 159.67 eV for Bi 4f 7/2 and 165.01eV for Bi 4f 5/2 as shown in Figure 4B which indicates the valence of Bi in the UB-30% was +3 (Bing et al., 2019). As depicted in Br3d spectra, the peaks at the binding energies of 68.68 and 69.80 eV represent Br 3d 5/2 and Br 3d 3/2 of BiOBr in UB-30% (Figure 4C) (Chen et al., 2019). The peaks of 530.43, 531.62 and 531.96 eV in O 1s spectra, are relevant to Bi-O and Zr-O, surface adsorption oxygen and hydroxyl groups, respectively composite (Figure 4D) (Gao et al., 2004). For the spectrum of C1s (Figure 4E), four binding energies at around 284.79, 285.74, 286.83 and 288.86 eV belong to the C=C (benzene ring), C-N (C–NH_2), C-C and C=O groups of U,

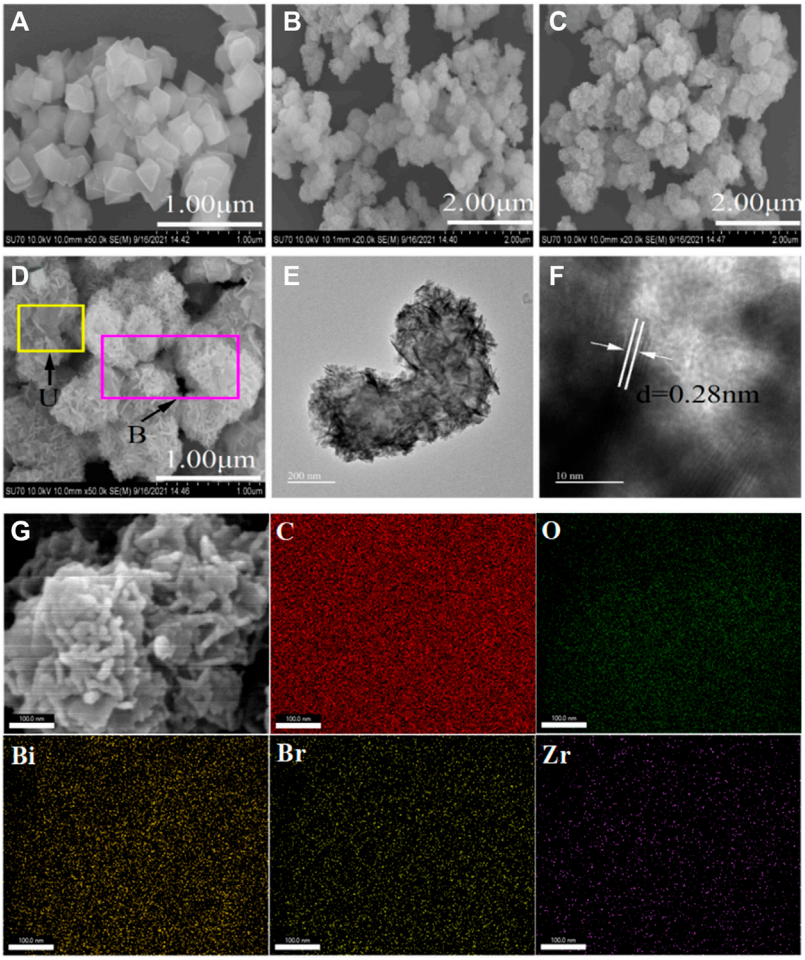

FIGURE 2
The morphologies of photocatalysts: SEM images of **(A)** U, **(B)** B and **(C,D)** UB-30%; TEM **(E)** and HRTEM **(F)** of UB-30%; EDS mapping of UB-30% **(G)**.

respectively (Su et al., 2017). The peaks of 182.62 eV, 185.30 eV in Zr 3d spectra, are relevant to Zr 3d 5/2 and Zr 3d 3/2 which indicates the existence of Zr^{4+} (Figure 4F). In addition to the Zr^{4+} characteristic at 182.62 and 185.30 eV, the Zr 3d spectrum of the composite has another significant peak at the center of 189.02 eV, which may be related to the interaction between Zr and the elements in B, thus proving the successful synthesis of the two substances (Zhao et al., 2021). The results of XPS further confirm the successful synthesis of BiOBr/UiO-66-NH_2 heterostructure, and the interface between U and B phase is tightly integrated.

Optical properties

Figure 5A shows the light response capabilities of U, B and UB-30% by UV-vis DRS. U has a good visible light response, it shows the strong absorption bands in the range of 200–490 nm. B shows the strong absorption bands in the range of 200–440 nm. The pure U exhibits an absorption edge at around 487 nm, and the pure BiOBr presents an absorption edge at about 443 nm. The combination of B with U causes the absorption edge of UB-30% to be red shifted (502 nm), it shows the strong absorption bands in the range of 200–500 nm. The visible light absorption range of the composite is larger than that of the two separate materials showing an improvement of the optical properties. It is beneficial for UB-30% to utilize light energy for photocatalytic reaction and improve the efficiency of photocatalytic degradation of pollutants.

The HOMO-LUMO (HOMO-LUMO energy level, collectively known as the Frontier orbit, refers to the Highest Occupied Molecular Orbital and the Lowest Unoccupied Molecular Orbital respectively) and band gap energy of U and B were calculated by the method of Tauc plot, which is based on the following Eq. 2

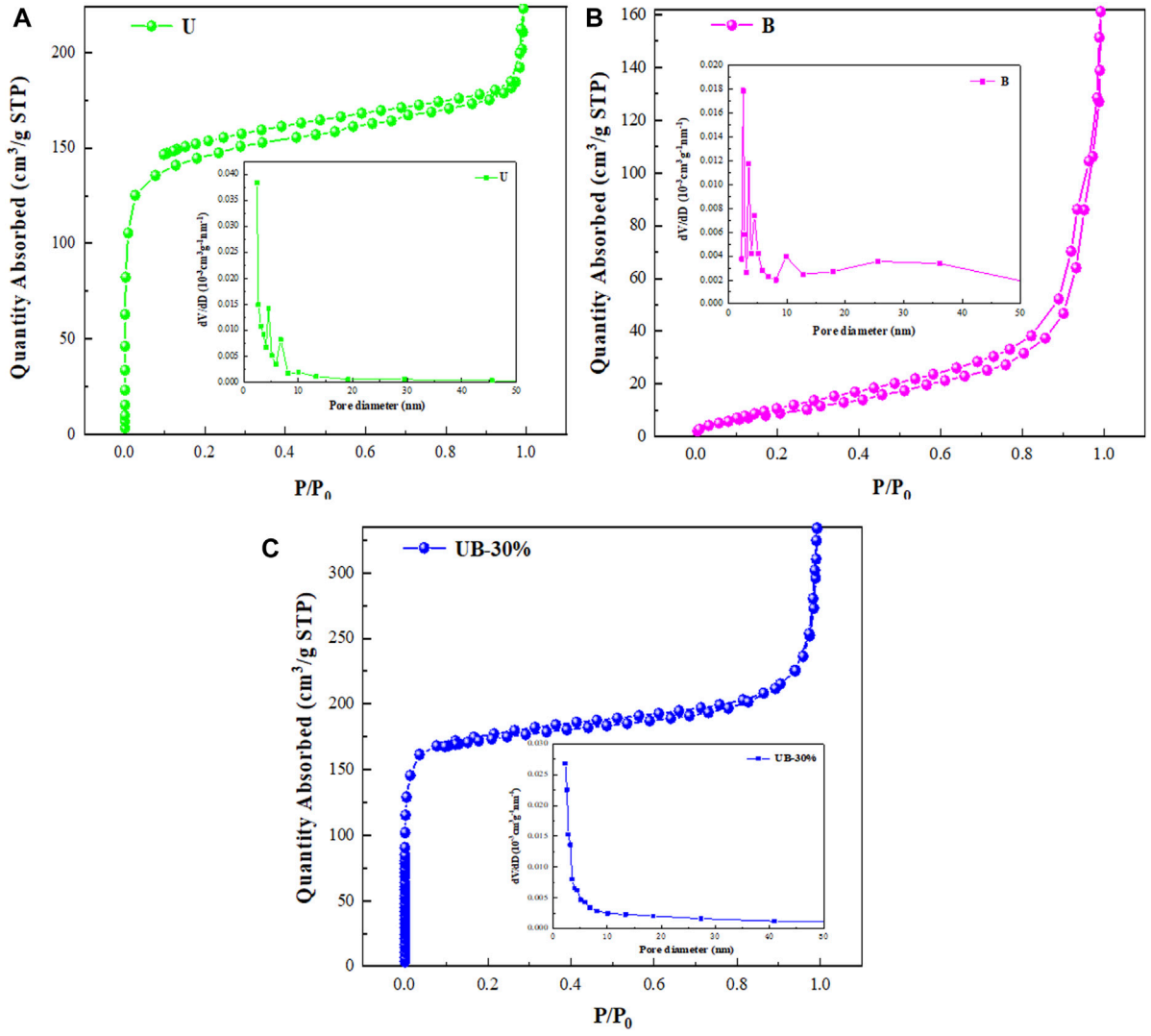

FIGURE 3
N_2 adsorption-desorption isotherm and aperture distribution of U **(A)**, B **(B)** and UB-30% composite **(C)**.

TABLE 1 The BET surface area (m^2/g), pore volumes (cm^3/g)and pore sizes (nm) of U, B and UB-30%.

	U	B	UB-30%
BET surface area	475	36	581
pore volume	0.14	0.73	0.26
pore size	2.26	8.07	2.38

$$\alpha h\nu = A\left(h\nu - Eg\right)^{n/2} \quad (2)$$

Where α, h, V, A and Eg are the optical absorption coefficient, Planck constant, light frequency, ratio and energy gap respectively. B and U are indirect gap semiconductors and direct gap semiconductors respectively, and their n values are 4 and 1, respectively. It can be seen from Figures 5B,C, the HOMO-LUMO gap and the band gap of U and B are 2.92 and 2.64 eV, respectively.

Photocatalytic activity of RhB

Before the photodegradation experiment, dark adsorption experiment was conducted for different samples for 1 h (Figure 6A). It can be seen that B and composite UB-50% have strong adsorption effect on RhB, and the adsorption equilibrium is not reached in 1 h. Combined with the SEM and pore analysis results above, the reason for the strong

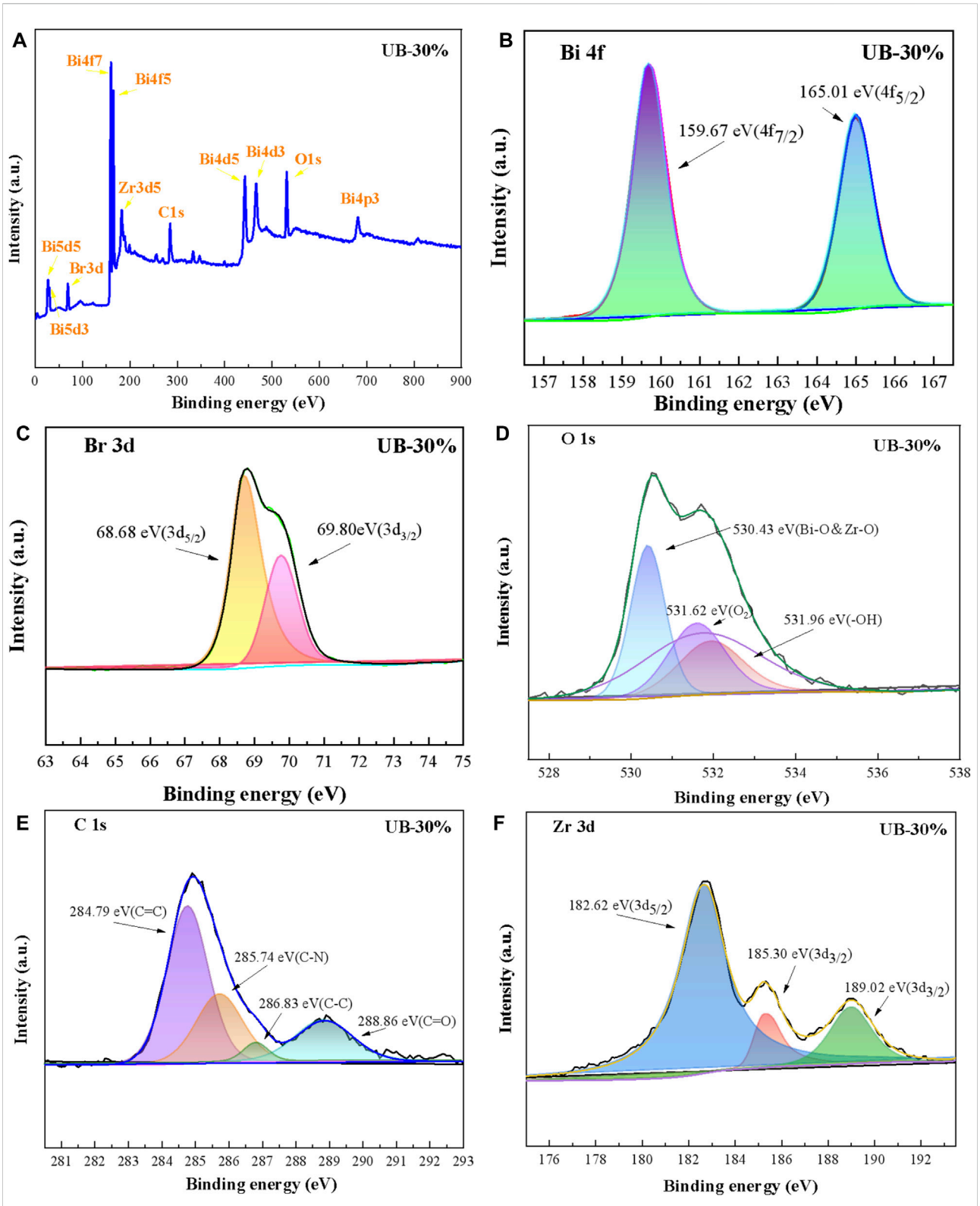

FIGURE 4
XPS spectra of UB-30% **(A)** the full spectrum of UB-30%; the spectra of UB-30%: **(B)** Bi 4f; **(C)** Br 3d; **(D)** O1s; **(E)** C1s; **(F)** Zr 3d.

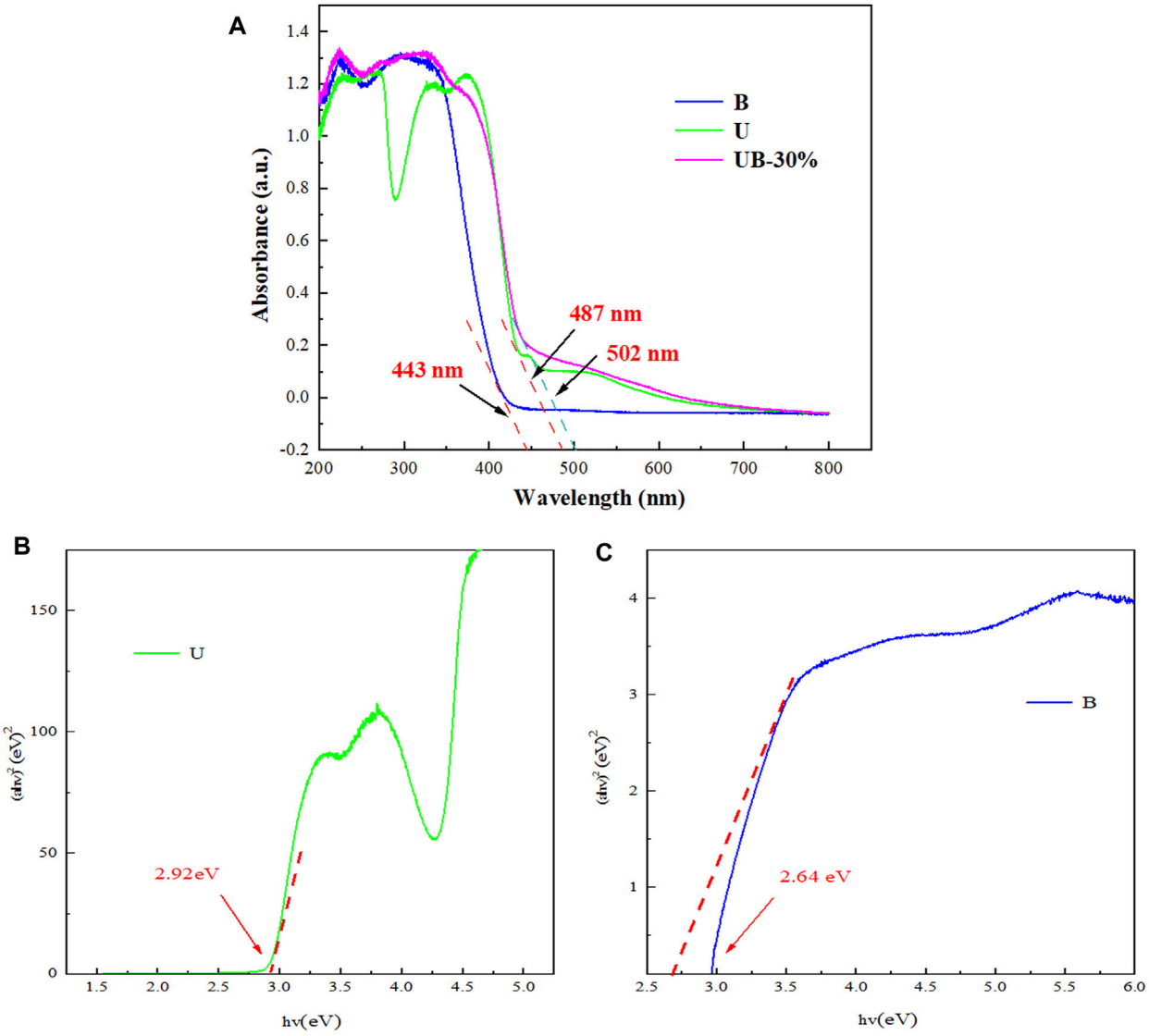

FIGURE 5
(A) UV-vis DRS of U, B and UB-30% composites; the bandgap energies of U **(B)** and B **(C)** versus the light energy.

adsorption capacity of B may be due to its unique 3D nanosphere structure. A large number of nanosheets are piled up to cause a large number of gaps and enhance their adsorption capacity. It is well known that the removal of RhB is achieved by adsorption and photocatalytic degradation, but photocatalytic process accounts for a larger proportion. If the dark adsorption is not close to equilibrium, there will be great interference for the subsequent determination of photodegradation efficiency. However, UB-X% (X = 10, 20, 30) can quickly reach the dark adsorption equilibrium of pollutants within 30min, the whole reaction time was shorten. It proved that U in the three composites effectively inhibited the adsorption capacity of B (Figure 6A), which is consistent with the results of pore size analysis and further proves that the two substances successfully combined to form a heterojunction. Meanwhile, the interference of B adsorption on the determination of light degradation ability of composite was eliminated. After determining the equilibrium time of adsorption and desorption by dark adsorption experiment, the removal efficiency of RhB by U and UB-X% (X = 10, 20, 30) were studied under simulated visible light irradiation (Figure 6B). When the prepared photocatalysts were added to the solution under visible light, RhB concentration decreases significantly, which indicates that they all had excellent visible light photocatalytic activity. RhB concentration not decreases significantly in the absence of catalyst (Blank), indicating that the self-degradation of RhB

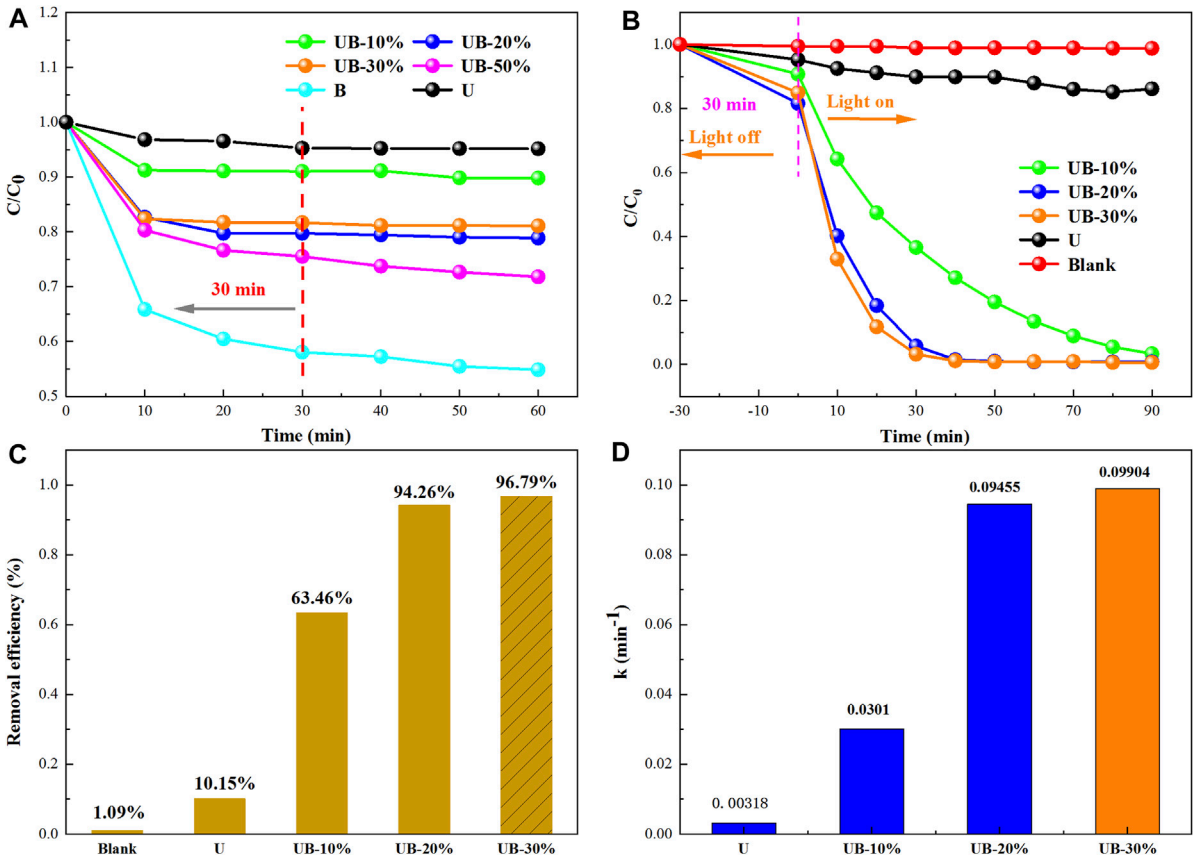

FIGURE 6
(A) dark adsorption of RhB; **(B)** photocatalytic degradation of RhB over as-prepared photocatalysts under visible light irradiation; **(C)** the removal efficiency of RhB by as-prepared photocatalysts after visible light irradiation for 30min; **(D)** the reaction rate constant k value after first-order kinetic fitting.

could be ignored. After dark adsorption, photocatalytic test was carried out for 90 min, and the removal rate of U is 13.86%. The photocatalytic activity of UB-X% (X = 10, 20, 30) are significantly higher than that of U, which improves the photocatalytic performance of U. Combined with dark adsorption experiments, it can be concluded that UB-30% is the best catalyst, which has less adsorption capacity for RhB and the highest photodegradation efficiency for RhB. Under visible light irradiation for 30min, the removal rate of UB-30% on RhB reached 96.79%, and that of 90min reached 99.37%, indicating that the dye was almost completely degraded, which was 7-fold greater than that of U. As can be seen in Figure 6C, the removal effects of U and UB-x % (X = 10, 20, 30) on RhB within 30min of visible light irradiation were compared, and it was more intuitive to compare that UB-30% had the best degradation effect on RhB within a short time of visible light irradiation.

RhB removal rate was fit for the pseudo-first-order reaction by using the equilibrium concentration as the initial concentration (Eq. 3).

$$\ln\left(\frac{C_0}{C}\right) = -kt \tag{3}$$

The corresponding reaction rate constants were 0.00318, 0.0301, 0.09455, and 0.09904 min^{-1} for U, UB-10%,UB-20% and UB-30%, respectively (Figure 6D). It further proved that UB-30% is the best degradation effect on RhB.

It can be concluded from the above study that when RhB concentration is 10 mg/L, UB-30% has a good photodegradation capacity. However, the concentration of dye pollutants in the actual water is not only 10 mg/L, so the same amount of UB-30% was put into RhB solutions with different concentration gradients to explore its degradation ability. Figure 7 shows the degradation of pollutants with different concentrations under visible light irradiation. On the whole, the degradation rate gradually slows down with the increase of pollutant concentration. But for 20 mg/L, 30 mg/L pollutant concentration, although the degradation rate were somewhat slowed down, it still had strong degradation effect after visible light irradiation for 90 min, and the removal rate of RhB can reach 98%. Because

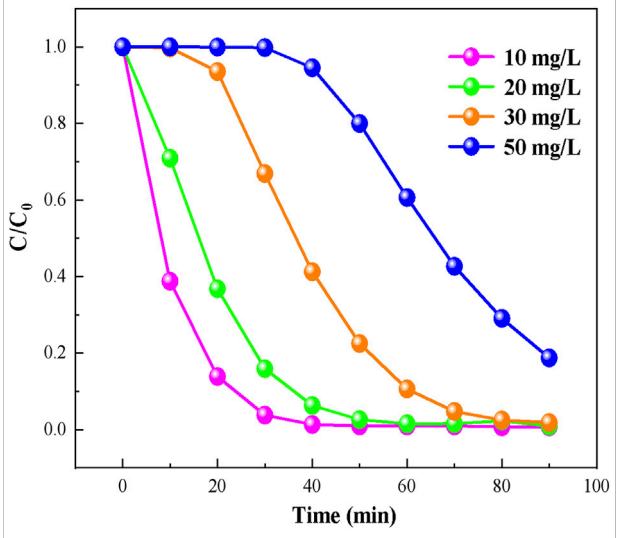

FIGURE 7
Degradation effect by UB-30% under different RhB concentrations.

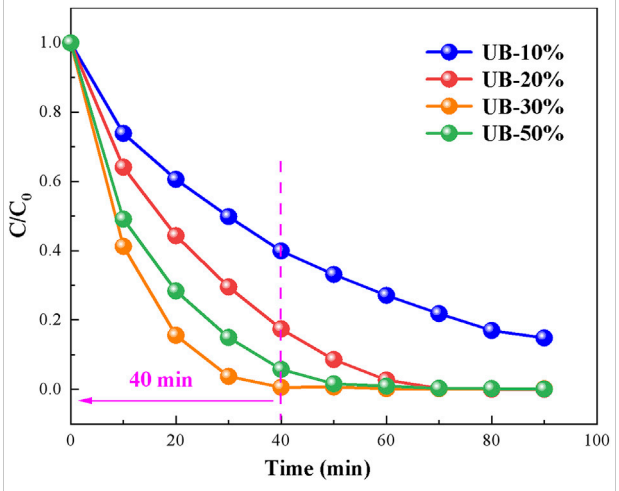

FIGURE 8
Photocatalytic degradation of RhB by photocatalyst prepared under direct visible light irradiation.

the active substances produced in the photocatalytic process reached a certain degradation limit, they were not enough to remove all the pollutants. It can also be clearly seen that when the concentration of pollutants was 50 mg/L, compared with other concentrations, the final removal effect of RhB was significantly reduced, and the degradation rate was also significantly slowed down. Within 40 min of light irradiation, little amount of RhB was removed, but the removal rate of pollutants was gradually enhanced as the photocatalytic reaction continued. It may be that with the advancement of the degradation process, the concentration of pollutant was reduced to the range that the catalyst can handle, leading to the enhancement of the removal effect. Even though the removal rate of high concentration was reduced, the removal rate of RhB can still reached more than 80%. It can be seen from the above experiments that UB-30% can effectively degrade RhB of different concentrations. When the concentration of RhB was low, the photocatalytic degradation of RhB was better.

According to the above studies, the prepared composite materials had excellent visible light response ability, and had a strong degradation ability to RhB in the conventional photocatalytic degradation reaction process. However, the reaction time of conventional photocatalytic reaction is too long, which is not conducive to the practical application of photocatalyst. Therefore, this study attempted to abandon the dark adsorption stage and directly carried out the photocatalytic reaction under visible light, to investigate whether UB-X% (X = 10, 20, 30,50) can efficiently and rapidly degrade RhB under a short time of visible light irradiation. As can be seen from Figure 8, under direct visible light irradiation, UB-X% (X = 10, 20, 30,50) showed excellent RhB removal ability. Among them, UB-30% can remove 99.43% RhB after visible light irradiation for only 40min, so as to achieve the purpose of efficient and rapid degradation of pollutants in a short time. In addition to UB-30%, the removal rate of UB-X % (X = 20,50) can also rearch more than 95% after visible light irradiation for 60min. Compared with the other three composite materials, the removal ability of UB-10% on RhB is poor, which may be due to the lack of photogenic electron holes, U and B do not reach a good coupling degree, resulting in the ability of heterojunction to inhibit e^--h^+ recombination was limited.

Reusability and stability

It is very important for a photocatalyst to have stability during recycling, which will affect the application of the catalyst in practical conditions. In order to explore the reusability of photocatalyst, five cycles were carried out. Before the experiment, the catalyst UB-30% participating in the photocatalytic reaction process was regenerated, mainly using ethanol for ultrasonic washing, drying in the oven at 90°C for 24 h, and the regenerated catalyst was used in the new photocatalytic degradation experiment of RhB. All other experimental conditions remained unchanged. As shown in Figure 9, the photodegradation efficiency of RhB in the first cycle after the reaction is 97.66 and 77.39% after five cycles, indicating that the photocatalyst has good reusability as a whole.

Enhanced visible-light photocatalytic activity mechanism

Figures 10A,B shows the UPS results for U and B. The work functions of U and B were -5.76 eV and -6.42 eV, respectively.

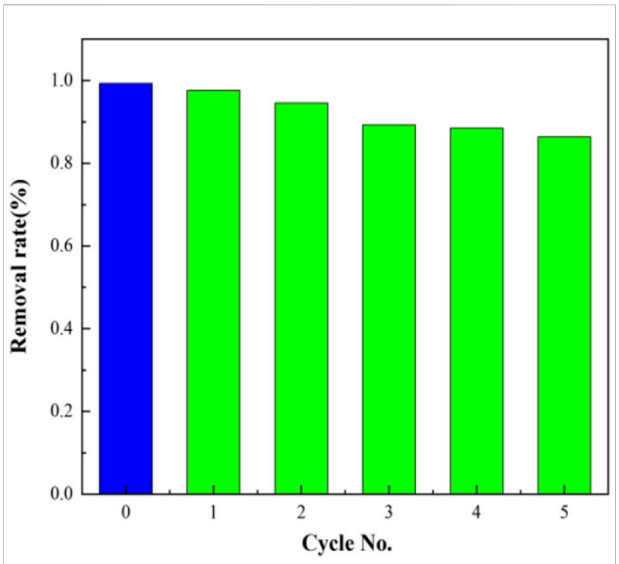

FIGURE 9
Reusability of UB-30% after five cycles of photodegradation of RhB.

The distances between the valence band (E_{VB}) position of U and B and the work function were -8.25 eV and -9.09 eV, respectively. Therefore, the HOMO potential of U and E_{VB} potential of B were estimated to be +2.49 eV and +2.65 eV, respectively. The conduction band (E_{CB}) potentials of the photocatalysts could be deduced by the following Eq. 4

$$E_{CB} = E_{VB} - E_g \quad (4)$$

where E_V and E_C are the corresponding E_{VB} and E_{CB} potential values. The LUMO potential of U and E_{CB} potential of B were -0.43 eV and +0.01 eV respectively. U and B possessed overlapping band potentials, implying that the two materials can be matched to synthesize a valid heterojunction.

In the above study, U and B had overlapping band potentials, which indicated that the two materials can be matched to synthesize a heterojunction. Photoexcited electrons (e^-) and holes (h^+) can transfer between them, resulting in the separation of their electron-hole pairs and inhibiting the their recombination. A series of photoelectrochemical tests were performed to verify the effect of photoexcited electron-hole pairs transfer and inhibition of recombination (Figure 11). Figure 11A shows the PL spectroscopy of the U, B and UB-30%. The strength of UB-30% PL is obviously weaker than that of U and B. Weak PL strength indicates weak electron-hole pair recombination. The combination of U and B is beneficial to inhibit the recombination of electron-hole pairs. EIS can be used to analyze the charge transfer resistance. As can be seen in Figure 11B, the radius of UB-30% Nyquist arc is smaller than U, indicating that the charge transfer resistance of UB-30% is small. Figure 11C shows the PC response of the U, B and UB-30% under simulated sunlight irradiation. Obviously, UB-30% shows the highest photocurrent response, which indicates a more efficient carriers transfer process and a longer photogenerated electron-hole pairs lifetime (Wang et al., 2021).

In addition, in order to study the photocatalytic degradation mechanism of RhB, the radical trapping experiments were carried out. Generally, the active radicals (·OH, h^+, and $\cdot O_2^-$) are responsible for RhB removal. Trapping experiments were performed, and different types of radical trapping reagents such as BQ, EDTA-2Na, and IPA were used to detect $\cdot O_2^-$, h^+, and ·OH, respectively. As seen in Figure 11D, the photodegradation of RhB is dramatically restrained when BQ and EDTA-2Na radical scavengers are introduced into the photocatalytic systems. However, the

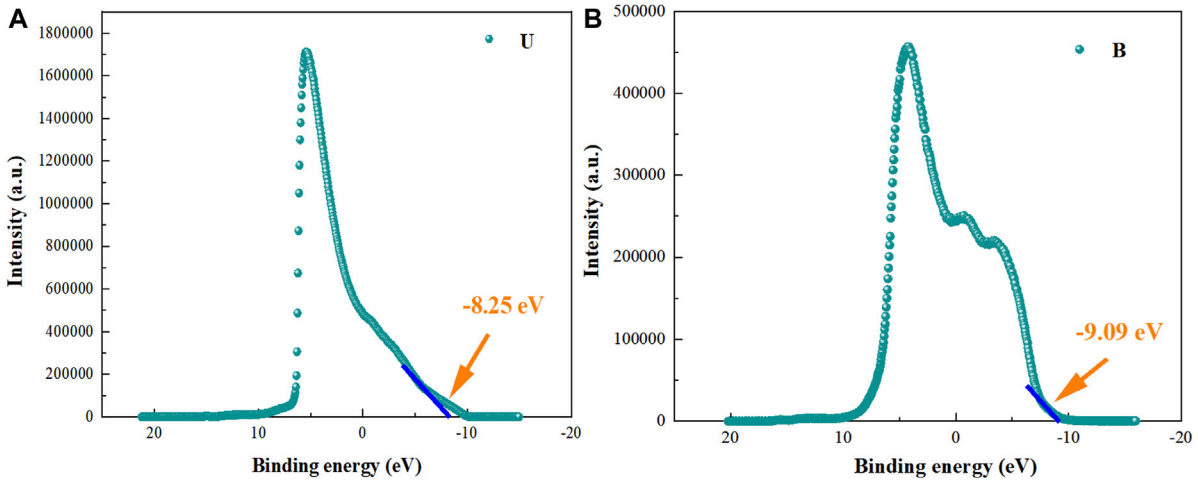

FIGURE 10
The UPS results for U **(A)** and B **(B)**.

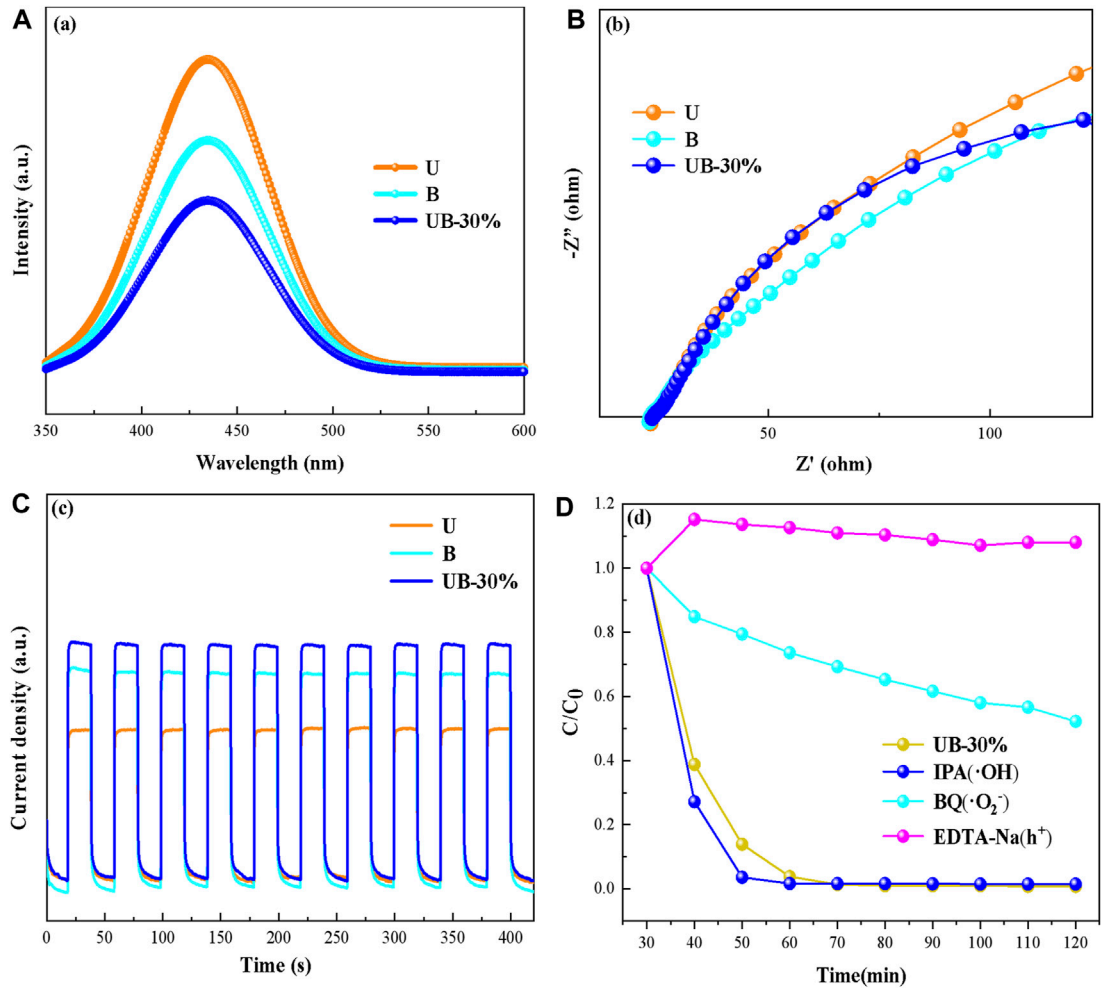

FIGURE 11
The photoelectrochemical tests, PL spectra **(A)**, EIS **(B)**, and PC **(C)** of U, B and UB-30%, respectively; the results of trapping experiments **(D)**.

degradation efficiency was slightly increased when IPA added. The above trapping results suggests that photogenerated $\cdot O_2^-$ and h^+ play main roles in the photodegradation, while ·OH has little influence on the photocatalytic activity.

According to the above band energy level analysis, the LUMO of U was more negative than B, while the HOMO of U is more negative than B. Therefore, the e^- transferred from the LUMO of U to the CB of B, the h^+ transferred from the VB of B to the HOMO of U. The LUMO potential of U was more negative than φ ($O_2/\cdot O_2^-$) (+0.13 eV vs. NHE), consequently the e^- on the LUMO of U can deacidize O_2 to $\cdot O_2^-$. But the h^+ on the VB of B can not oxidize H_2O to form ·OH, because E_{VB} of B does not have a higher positive potential than standard $OH^-/\cdot OH$ (2.68 eV vs. NHE). Similarly, the h^+ on the HOMO of U can not oxidize H_2O to form ·OH. According to the results of trapping experiments, the h^+ degrade RhB directly. Base on the above studies, the photocatalytic degradation mechanism was proposed in Figure 12. The whole RhB degradation process can be summarized by the following reaction formula:

$$UiO-66-NH_2 + hv \rightarrow UiO-66-NH_2(h^+ + e^-) \quad (5)$$

$$BiOBr + hv \rightarrow BiOBr(h^+ + e^-) \quad (6)$$

$$UiO-66-NH_2(e^-) + O_2 \rightarrow UiO-66-NH_2 + O_{2^-} \quad (7)$$

$$RhB + O_{2^-}, h^+(BiOBr/UiO-66-NH_2) \rightarrow CO_2 + H_2O \quad (8)$$

Conclusion

In conclusion, BiOBr/UiO-66-NH_2 heterojunctions with different proportions were successfully synthesized by simple *in-situ* deposition method. The composite material had good visible light response capability and inhibited electron-hole pair recombination. Meanwhile, the construction of composite material inhibited the adsorption of 3D spherical BiOBr. The balance of adsorption-desorption can be achieved in a short time and the whole reaction

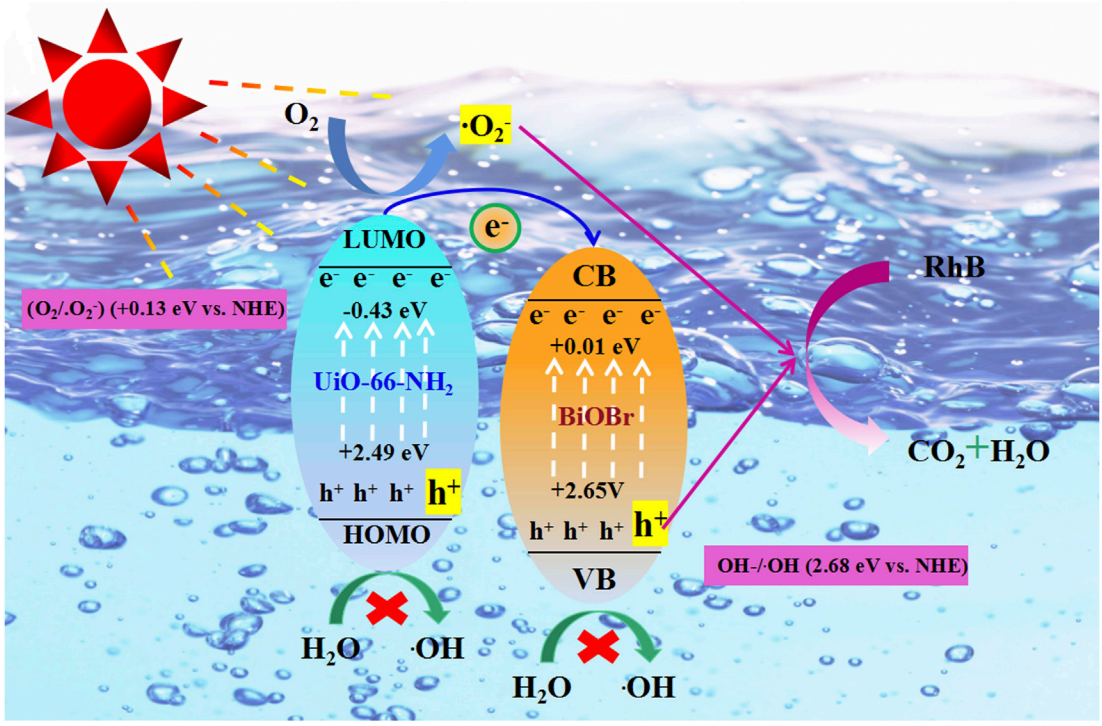

FIGURE 12
The plausible photodegradation mechanism of RhB over UB-30% composite under simulated sunlight irradiation.

time can be shortened. Under simulated light conditions, the composite materials with different ratios of RhB dye had excellent degradation effect, and UB-30% had the highest photodegradation performance of RhB, and the degradation efficiency was up to 99%. Even with the increase of pollutant concentration, UB-30% still exhibited excellent photocatalytic ability. Abandoning the dark adsorption stage, the prepared material can remove 99.43% RhB after visible light irradiation for only 40 min, but it was only at a preliminary stage of exploration. Free radical scavenging experiments showed that $\cdot O_2^-$ and h^+ were the main free radicals in the whole degradation process. Finally, the photocatalytic enhancement mechanism is proposed by combining photochemical test.

Data availability statement

The original contributions presented in the study are included in the article/supplementary material further inquiries can be directed to the corresponding author.

Author contributions

Conceptualization, SF and YZ; methodology, SF; software, QN; validation, SF, YZ, and ZY; formal analysis, SF; investigation, SF, YZ, and ZY; resources, YZ and ZY; data curation, SF and QN.; writing—original draft preparation, SF; writing—review and editing, SF; visualization, supervision, YZ and ZY; project administration, YZ; funding acquisition, YZ All authors have read and agreed to the published version of the manuscript.

Funding

This research was supported by Liaoning Revitalization Talents Program (XLYC1807045) and Shenyang Youth Science, Technology Innovation Talents Support Plan (RC180101).

Acknowledgments

We thank the Key Laboratory of Clean Energy, Liaoning Province and Shenyang Aerospace University College of Energy and Environment for their scientific research assistance.

Conflict of interest

The authors declare that the research was conducted in the absence of any commercial or financial relationships that could be construed as a potential conflict of interest.

Publisher's note

References

Bargozideh, S., Tasviri, M., Shekarabi, S., and Daneshgar, H. (2020). Magnetic $BiFeO_3$ decorated UiO-66 as a p–n heterojunction photocatalyst for simultaneous degradation of a binary mixture of anionic and cationic dyes. *New J. Chem.* 44, 13083–13092. doi:10.1039/d0nj02594a

Bhatt, A. S., Sakaria, P. L., Vasudevan, M., Pawar, R. R., Sudheesh, N., Bajaj, H. C., et al. (2012). Adsorption of an anionic dye from aqueous medium by organoclays: Equilibrium modeling, kinetic and thermodynamic exploration. *RSC Adv.* 2, 8663–8671. doi:10.1039/c2ra20347b

Bing, X. M., Jian, X. Y., Chu, J. H., Li, J., and Guo, C. Y. (2019). Hierarchically porous $BiOBr/ZnA_{l1.8}Fe_{0.2}O_4$ and its excellent adsorption and photocatalysis activity. *Mat. Res. Bull.* 110, 1–12. doi:10.1016/j.materresbull.2018.10.006

Chen, Y., Qian, J., Wang, N., Xing, J., and Liu, L. (2020). *In-situ* synthesis of CNT/TiO_2 heterojunction nanocomposite and its efficient photocatalytic degradation of Rhodamine B dye. *Inorg. Chem. Commun.* 119, 108071. doi:10.1016/j.inoche.2020.108071

Chen, Y. Z., Guo, D. J., Yang, H. T., Liu, D. N., and Zhai, Y. L. (2019). Solvothermal synthesis of biochar@$ZnFe_2O_4$/BiOBr Z-scheme heterojunction for efficient photocatalytic ciprofloxacin degradation under visible light. *Appl. Surf. Sci.* 493, 1361–1367. doi:10.1016/j.apsusc.2019.04.160

Fan, G., Zhan, J., Luo, J., Lin, J., Qu, F., Du, B., et al. (2021). Fabrication of heterostructured Ag/AgCl@g-C3N4@UiO-66(NH_2) nanocomposite for efficient photocatalytic inactivation of Microcystis aeruginosa under visible light. *J. Hazard. Mat.* 404, 124062. doi:10.1016/j.jhazmat.2020.124062

Gao, X. Y., Wang, S. Y., Li, J., Zheng, Y. X., Zhang, R. J., Zhou, P., et al. (2004). Study of structure and optical properties of silver oxide films by ellipsometry, XRD and XPS methods. *Thin Solid Films* 455–456, 438–442. doi:10.1016/j.tsf.2003.11.242

Han, L. P., Li, B., Wen, H., Guo, Y. X., and Lin, Z. (2021). Photocatalytic degradation of mixed pollutants in aqueous wastewater using mesoporous 2D/2D TiO_2(B)-BiOBr heterojunction. *J. Mat. Sci. Technol.* 70, 176–184. doi:10.1016/j.jmst.2020.08.036

Hao, X. L., Yu, X. J., Li, H. Y., Zhang, Z. Y., Wang, Y., and Li, J. Y. (2020). The preparation of full-range BiOBr/BiOI heterojunctions and the tunability of their photocatalytic performance during the synthesis of imines under visible light irradiation. *Appl. Surf. Sci.* 528, 147015. doi:10.1016/j.apsusc.2020.147015

Liu, Z. W., Zhuang, Y. L., Dong, L. M., Mu, H. X., Tian, S., Wang, L. M., et al. (2022). Preparation of CeO_2/UiO-66-NH_2 heterojunction and study on a photocatalytic degradation mechanism. *Materials* 15, 2564. doi:10.3390/ma15072564

Shi, X., Wang, P. Q., Wu, Y. J., Xing, X., and Bai, Y. (2019). Ternary heterostructural $BiOBr_{0.5}I_{0.5}$/BiOBr/BiOI engineering for efficient photocatalytic NO removal via synergistic effects of enhanced carrier and exciton photocatalysis. *J. Mat. Sci. Mat. Electron.* 30, 19154–19163. doi:10.1007/s10854-019-02272-2

Su, Y., Zhang, Z., Liu, H., and Wang, Y. (2017). $Cd_{0.2}Zn_{0.8}S$@UiO-66-NH_2 nanocomposites as efficient and stable visible-light-driven photocatalyst for H_2 evolution and CO_2 reduction. *Appl. Catal. B Environ.* 200, 448–457. doi:10.1016/j.apcatb.2016.07.032

Sun, Y., Chen, M., Liu, H., Zhu, Y., Wang, D., and Yan, M. (2020). Adsorptive removal of dye and antibiotic from water with functionalized zirconium-based metal organic framework and graphene oxide composite nanomaterial UiO-66-$(OH)_2$/GO. *Appl. Surf. Sci.* 525, 146614. doi:10.1016/j.apsusc.2020.146614

Wang, K., Xing, Z. P., Meng, D., Zhang, S. Y., Li, Z. Z., Pan, K., et al. (2021). Hollow $MoSe_2$@Bi_2S_3/CdS core-shell nanostructure as dual Z-scheme heterojunctions with enhanced full spectrum photocatalytic-photothermal performance. *Appl. Catal. B Environ.* 281, 119482. doi:10.1016/j.apcatb.2020.119482

Wen, J., Liu, H., Zheng, Y., Wu, Y., and Gao, J. (2020). A novel of PTA/ZIF-8@Cellulose aerogel composite materials for efficient photocatalytic degradation of organic dyes in water. *Z. Anorg. Allg. Chem.* 646, 444–450. doi:10.1002/zaac.202000096

Wu, H., Yildirim, T., and Zhou, W. (2013). Exceptional mechanical stability of highly porous zirconium Metal–Organic framework UiO-66 and its important implications. *J. Phys. Chem. Lett.* 4, 925–930. doi:10.1021/jz4002345

Xia, Z., Shi, B., Zhu, W., and Lü, C. (2021). Temperature-responsive polymer-tethered Zr-porphyrin MOFs encapsulated carbon dot nanohybrids with boosted visible-light photodegradation for organic contaminants in water. *Chem. Eng. J.* 426, 131794. doi:10.1016/j.cej.2021.131794

Xu, X. Y., Chu, C., Fu, H. F., Du, X. D., Wang, P., Zheng, W. W., et al. (2018). Light-responsive UiO-66-NH_2/Ag_3PO_4 MOF-nanoparticle composites for the capture and release of sulfamethoxazole. *Chem. Eng. J.* 350, 436–444. doi:10.1016/j.cej.2018.06.005

Yang, X., Feng, T. J., He, S., Fu, M., Niu, X., Zhang, T., et al. (2019). Flower-like BiOBr/UiO-66-NH_2 nanosphere with improved photocatalytic property for norfloxacin removal. *Chemosphere* 220, 98–106. doi:10.1016/j.chemosphere.2018.12.086

Yang, X. Z., Wu, T., Gao, P. P., Zhu, G. F., and Fan, J. (2020). Novel approach for preparation of three-dimensional BiOBr/BiOI hybrid nanocomposites and their removal performance of antibiotics in water. *Colloids Surfaces A Physicochem. Eng. Aspects* 605, 125344. doi:10.1016/j.colsurfa.2020.125344

Yang, Z. C., Zhao, W., Liu, C. X., Qian, X. X., Chang, W. Y., Sun, T., et al. (2021). Construction of porous-hydrangea BiOBr/BiOI n-n heterojunction with enhanced photodegradation of tetracycline hydrochloride under visible light. *J. Alloys Compd.* 864, 158784. doi:10.1016/j.jallcom.2021.158784

Zeng, L., Guo, X. Y., He, C., and Duan, C. Y. (2016). Metal-organic frameworks: Versatile materials for heterogeneous photocatalysis. *ACS Catal.* 6, 7935–7947. doi:10.1021/acscatal.6b02228

Zhang, X. L., Zhang, N., Gan, C. X., Liu, Y. F., Chen, L., Zhang, C., et al. (2019). Synthesis of In_2S_3/UiO-66 hybrid with enhanced photocatalytic activity towards methyl orange and tetracycline hydrochloride degradation under visible-light irradiation. *Mat. Sci. Semicond. process.* 91, 212–221. doi:10.1016/j.mssp.2018.11.014

Zhao, C., Li, Y., Chu, H., Pan, X., Ling, L., Wang, P., et al. (2021). Construction of direct Z-scheme Bi_5O_7I/UiO-66-NH_2 heterojunction photocatalysts for enhanced degradation of ciprofloxacin: Mechanism insight, pathway analysis and toxicity evaluation. *J. Hazard. Mat.* 419, 126466. doi:10.1016/j.jhazmat.2021.126466

Zhou, Y. C., Wang, C. C., Wang, P., Fu, H. F., and Zhao, C. (2020). *In-situ* photochemical reduction of Ag-UiO-66-NH_2 composite for enhanced photocatalytic performance. *Chin. J. Inorg. Chem.* 36, 2100–2112. doi:10.11862/CJIC.2020.207

Zhu, H., Gong, L., Chen, Z., Hu, Y., and Li, Z. (2020). Al cluster oxide modified a hematite/P3HT ternary Z-scheme photocatalyst with excellent photocatalytic performance: A discussion of the mechanism. *J. Hazard. Mat.* 391, 122252. doi:10.1016/j.jhazmat.2020.122252